Microchimica Acta (2022) 189: 64
https://doi.org/10.1007/s00604-022-05162-3

ORIGINAL PAPER

# Fabrication of ionic liquid stabilized MXene interface for electrochemical dopamine detection

**Umay Amara[1,2] · Bilal Sarfraz[3] · Khalid Mahmood[2] · Muhammad Taqi Mehran[3] · Nawshad Muhammad[4] · Akhtar Hayat[1] · Mian Hasnain Nawaz[1]**

Received: 19 September 2021 / Accepted: 26 December 2021 / Published online: 17 January 2022


## Abstract

Development of MXene ($Ti_3C_2Cl_2$)-based sensing platforms by exploiting their inherent active electrochemistry is highly challenging due to their characteristic poor stability in air and water. Herein, we report a cost-effective methodology to deposit MXene on a conductive graphitic pencil electrode (GPE). MXenes can provide active surface area due to their clever morphology of accordion-like sheets; however, the disposition to stack together limits their potential applications. A task-specific ionic liquid (1-methyl imidazolium acetate) is utilized as a multiplex host material to engineer MXene interface via π-π interactions as well as to act as a selective binding site for biomolecules. The resulting IL-MXene/GPE interface proved to be a highly stable interface owing to good interactions between MXene and IL that inhibited electrode leaching and boosted electron transfer at the electrode–electrolyte interface. It resulted in robust dopamine (DA) oxidation with amplified faradaic response and enhanced sensitivity (9.61 μA $\mu M^{-1}$ $cm^{-2}$) for DA detection. This fabricated sensor demonstrated large linear range (10 μM – 2000 μM), low detection limit (702 nM), high reproducibility, and good selectivity. We anticipate that such platform will pave the way for the development of stable and economically viable MXene-based sensors without sacrificing their inherent properties.

**Keywords** MXene · Ionic liquid · Electrochemical sensor · Dopamine detection · MXene stability · Graphitic pencil electrode

## Introduction

Dopamine (DA) is a classical neuromodulator involved in the regulation of a multitude of neurological processes [1–3]. DA dysfunction has been implicated in the pathogenesis of many neurological disorders [4]. Therefore, DA homeostasis is the fingerprint of ongoing physiological conditions and neuronal health [5]. Many methods have been employed for active monitoring of DA dynamics but electrochemical sensors offer cost-effective [6], portable, and easy to operate assay platform with robust quantitative readouts [7–9]. However, electro-polymerization leading to biofouling is the major challenge associated with intrinsic transduction protocols which eventually causes device inactivation [10]. Likewise, many secondary reactions after electron transportation also produce insulating polymeric layers leading to electrode surface inactivation. Meanwhile, reduced selectivity owing to 100–1000 times higher concentrations and comparable oxidizing potentials of coexisting metabolites is also a great concern. Therefore, DA diagnostics require a sensing interface that selectively outputs DA signal with higher sensitivity, mechanical stability, and improved analytical performance [11].

In this regard, microstructures like MXene, a member of 2D transition metal nitrides, carbides, and carbonitrides

✉ Khalid Mahmood
khalidmahmood@bzu.edu.pk

✉ Mian Hasnain Nawaz
mhnawaz@cuilahore.edu.pk

[1] Interdisciplinary Research Centre in Biomedical Materials (IRCBM), COMSATS University Islamabad, Lahore Campus, Lahore 54000, Pakistan

[2] Institute of Chemical Sciences, Bahauddin Zakariya University, Multan 60800, Pakistan

[3] School of Chemical and Materials Engineering (SCME), National University of Sciences and Technology (NUST), Islamabad H-12, Pakistan

[4] Institute of Basic Medical Sciences, Khyber Medical University, Peshawar, Pakistan

bearing abundant surface termination groups (e.g., OH, F, Cl, and/or O) with well-defined morphologies, have induced enhanced sensitivity of sensing interface [12–14]. Accordion-like multilayer architecture of MXenes has been employed as a substrate layer in electrochemical sensors due to excellent conductivity and tunable band-gap owing to alternating surface functional groups [15–19]. Additionally, active surface area, biocompatibility, and hydrophilicity of MXenes made them more accessible to the target analyte [20, 21]. Moreover, MXenes have been reported to show resistivity against the fouling and passivation of electrodes [22, 23]. However, easy restacking, low flexibility, and substantially poor stability in aqueous media and air, stemming from hydrophilic functional groups, make them highly vulnerable to oxidation and limit the working potential range [24, 25].

Assembling MXenes sheets with other nanomaterials could be a possible solution to the aforesaid problems [26, 27]. Nevertheless, it is still a great challenge to generate stable nanoarchitecture without sacrificing some of their intrinsic properties. We tried to counter this challenge by using ionic liquids (IL), i.e., organic salts with intriguing properties like economic viability, wide solubility range, high ionic conductivity, ideal thermal stability, redox stability, and good biocompatibility. It eventually offers a plethora of design combinations by improving the properties of both the inorganic anions and organic cations, independently [28]. IL-integrated interfaces provide enhanced catalytic traits and stabilize reactive catalytic species thus adding a long-lasting stability to the fabricated sensors [29]. Moreover, excellent electrochemical conductivity, higher electron transfer kinetics, and good biocompatibility eventually enhance the transducing signals thereby decreasing the detection potential and improving the sensitivity of the developed interface [30–33]. Additionally, the economic viability, antifouling property, wide potential range, and ability to lower overpotential make them inimitable material for selective DA sensing [34–36]. In principle, the inherent surface functional groups of MXene can bond or adsorb biorecognition materials (IL) via π-π interactions leading to hierarchal microstructure with greater stability [37] and biocompatibility for DA sensing.

Herein, we investigated the effect of oxidative instability mitigation by MXenes' surface engineering against DA sensing performance. Exploiting surface functional groups of MXene, we propose that stabilization of its surface by IL (1-methylimidazolium acetate) could be an effective strategy to mitigate its oxidative degradation without compromising the highly conducive MXene core. The imidazole group acts as a selective DA-binding site to specifically analyze DA in complex biological systems. As imidazole ring is positively charged and electron-deficient, it can accept and withdraw electrons from dopamine to oxidize it. Meanwhile, the methyl group hydrogen on imidazole formed electrostatic interactions with MXene layers to enhance the stability and sensitivity of the designed interface with a lower detection limit. The developed interface proved to be highly resilient and stable with good reproducibility. Eventually, the sensor was employed to monitor DA in human serum samples as well, suggesting its reliability for the complex real sample applications.

## Experimental section

### Synthesis of MXene

MXene was prepared by mixing copper chloride and MAX phase precursor (6:1) in a vacuum glove box under an argon (Ar) environment. This mixed powder was then shifted into a boat crucible and placed in a tube furnace at 550 °C for 5 h under Ar gas protection for thermal treatment. The mixture was then treated with 5% HCl for 2 h under vigorous stirring for the removal of residues. The product was separated by centrifugation at 4000 (RPM), with several washes with DI water to maintain a pH greater than 6. Finally, the obtained product was washed with absolute ethanol and vacuum-dried overnight in an oven at 70–80 °C [38].

### Synthesis of 1-methyl imidazolium acetate ionic liquid (IL)

The ionic liquid was synthesized using a modified protocol previously reported by our group [39]. The 0.01 M 1-methylimidazole was neutralized using 0.01 M acetic acid in a two-necked flask at room temperature, followed by cooling and stirring for 6 h. The as-prepared IL was purified via rotary evaporator at 60 °C. The structure of IL was identified using 1HNMR spectroscopy (Bruker, 500 MHz, DMSO – d 6), with given proton 1H NMR chemical shifts: $\delta$: 7.60 (s, 1H, C2–H),7.12 (s, 1H, C4–H), 6.90 (s, 1H, C5–H), 4.35 (s, 1H, N2–H), 3.65 (s, 3H, N3–CH3), 1.92 (s, 3H, CH3COO).

### Surface modification of MXene with ionic liquid (IL-MXene)

IL-MXene nanoarchitecture was prepared by the ultra-sonication of a 1:1 mixture of MXene (1 mg/mL in DI water) and IL (1 mL) for 12 min. The ultra-sonication technique improved the dispersion of assembling host–guest molecules by acoustic cavitation and facilitated the π-π interactions for stable adduct formation [40, 41].

### Choice of the materials

Designing MXene-based sensors is a great challenge to the scientific community owing to the poor shelf life of

MXene in water and air, as MXene oxidizes to titanium oxide. So far, MXene fabrication without sacrificing its inherent conductive properties for the development of sensors has rarely been reported. Therefore, herein, we synthesized an IL-MXene-based sensor with good stability and excellent electrocatalytic efficacy. MXene provided active surface area, conducive support, and biocompatibility for the sensor. Meanwhile, IL acts as multiplex material to stabilize MXene and to adsorb biomolecule leading to sensitive and stable microstructure for DA sensing.

### Electrode fabrication for electrochemical studies

The synthesized MXene, IL, and IL-MXene nanoarchitecture was then used to fabricate the working interface, i.e., graphitic pencil electrodes (GPE) for DA screening. Before modification, the edge of GPE was cut with the cutter to obtain a smooth and clean working interface followed by washing with DI water. We have chosen GPE as a working electrode (2 mm) due to its easy availability, economic feasibility, and nominal pretreatment requirements. Besides, the graphitic surface of $sp^2$ carbon provides ease at fabrication and adsorption without employing any binder material. Typically, 2 µL of synthesized materials were drop-casted on the GPE to modify the working electrode interface and dried at medium temperature. After drying, the fabricated GPE was placed into the electrochemical cell system and screened against DA. Meanwhile, the IL-MXene/GPE interface was also analyzed under different concentrations of dopamine in PBS (7.4) with differential pulse voltammetry (DPV) in potential bounds of 0–0.8 V with a step size of 25 mV and pulse size of 250 mV. The same study was performed via amperometry by adding DA spike after every 50 s in an electrochemical cell with 20 mL PBS (7.4). All the electrochemical experiments were performed at a scan rate of 100 mV/s.

## Results and discussion

The morphology of the MAX phase ($Ti_3AlC_2$), MXene ($Ti_3C_2Cl_2$), and IL-MXene was evaluated via scanning electron microscopy. MAX phase showed a graphite-like stacked structure as expected for a bulk-layered ternary carbide [42] as displayed in Fig. 1A. However, MXene generated via a Lewis acid salt route depicted a multi-layered accordion-like structure in accordance with previously reported MXenes obtained via HF etching [43]. This expanded the accordion-like morphology possibly due to excessively escaped gasses ($H_2$ in this case). Meanwhile, the flat edges of MXene represented good interactions between MXene stacks probably due to the possibility of inter-flakes H-bonding, as shown in Fig. 1B [44]. Moreover, the interlayer spacing in MXene flakes provided a more accessible area for chemical activity compared to the 3-D MAX phase, as could be perceived from the inset of Fig. 1B.

From these micrographs, the average diameter of individual MXene flake is perceived to be 0.1 µm which is comparable to the reported literature [45–47]. However, a uniform distribution of the IL is seen on MXene after IL deposition as shown in Fig. S1A. The elemental map analysis and EDS spectrum of IL-MXene exhibited distinct peaks of carbon (45%), chlorine (20%), titanium (22%), and copper (13%) as shown in Fig S1B and C.

XRD patterns of the MAX phase, MXene, and IL-modified MXene are shown in Fig. S2. The diffraction peaks (002), (004), (008), (104), and (105) at 2□ values of 9.5, 19.1, 34, 38.95, and 41.7 respectively, corresponded to the MAX precursor as revealed in Fig. S2A(a). Meanwhile, the (002), (004), and (008) peaks were downshifted to 7.5, 16.15, and 32.15, respectively, in MXene from the MAX phase, as shown in Fig. S2A(b). This shift was due to a larger lattice constant and an increase in interlayer space between MXene stacks after Al etching [38, 44]. While peaks (104) and (105) were moved towards higher 2□ at 43.3 and 39.7, respectively, while the intensity of (104) peak was reduced. The (006) peak was visible at a 2□ value of 28.5. All the peaks in the MAX phase and

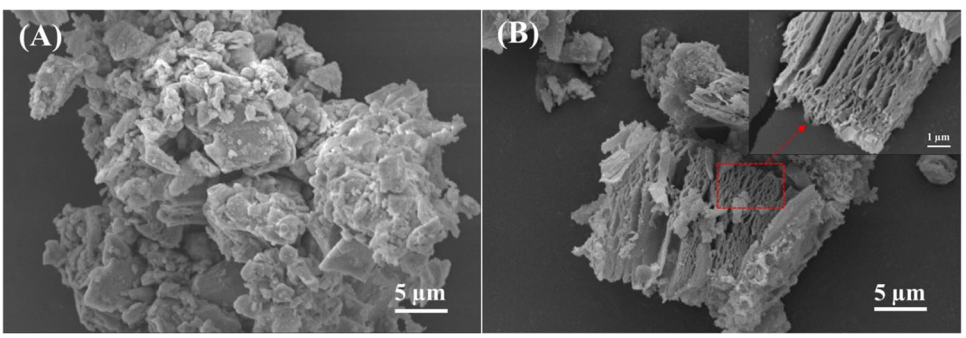


**Fig. 1** Scanning electronic microscopy of **A** MAX phase, **B** MXene. Samples were prepared via reported methodology discussed previously and deposited on glass slides via drop-casting for further scanning

MXene were well consistent with reported data. However, diffraction peaks at (002), (004), (006), (008), (104), and (105) were moved towards higher 2□ values of 10.2, 20.1, 28.9, 35.3, 42.3, and 45.9, respectively, as presented in Fig. S2A(c). The shift in scanning angle was owed to good intercalations among IL and 2D MXene sheets. The prominent diffraction peak at 24.46 corresponded to IL molecule [48].

The surface defects of the MXene before and after fabrication with IL were examined through Raman spectrum. The peak at 1359 $cm^{-1}$ named as D-band corresponded to surface defects and disorders in a graphitic matrix. Meanwhile, the peak at 1587 $cm^{-1}$ corresponded to $sp^2$-hybridized carbon of the graphitic skeleton and called as G-band as envisioned in Fig. S2B(d). The peak ratio ($I_D$/$I_G$) was calculated to be 0.67 for pristine MXene. These high-intensity peaks and ratio indicated the effectiveness of the Lewis acid synthetic route to get MXene with high surface area. However, the intensity of the D and G bands decreased after stabilizing MXene with IL molecules as could be seen from Fig. S2B(e). Consequently, the ($I_D$/$I_G$) increased to 0.7 owing to the larger degree of disorder. These results were consistent with microscopic (SEM) findings. Moreover, the shift in D and G bands was witnessed in IL-MXene as was observed in the case of XRD. The shift corroborated the presence of good interacting forces in integrated nano-adduct thus leading to the development of a highly stabilized surface.

## Electrochemical investigation of modified interfaces

Cyclic voltammetry (CV) and Electrochemical Impedance Spectroscopy (EIS) experiments were performed to analyze the electron transportation capability of designed interfaces in 5 mM redox probe $(Fe[CN]6)^{4-/3-}$ in the applied potential boundaries of (− 0.6 to 0.8 V). In the cyclic voltammetry responses, Fig. 2A(a) revealed that the peak-to-peak separation value (ΔEp) for bare GPE electrode was much higher (0.28 V) with a lower current (28.1 µA), owing to the poor electron transfer. The faradic response was enhanced (41.8 µA) with decreased ΔEp (0.26) in case of pristine IL, as shown in Fig. 2A(b). However, a substantial increase in peak current (97.8 µA) with decreased ΔEp (0.22) was observed in case of pristine MXene, indicating the improved interfacial redox process due to its conductive accordion-like expanded layers that enhanced the active surface area and aided electron transfer, as shown in Fig. 2A(c). Moreover, decoration of IL-MXene nano-adduct on electrode interface radically enhanced the faradic response with decreased ΔEp (0.21 V), as revealed in Fig. 2A(d). This decreased redox peak separation and increased oxidation current (160.9 µA) could be ascribed to the stable film formation with massive catalytically active sites that enhanced electrochemically active surface area [49]. Likewise, the imidazolium nitrogen of IL also contributed to the amplification of faradaic current.

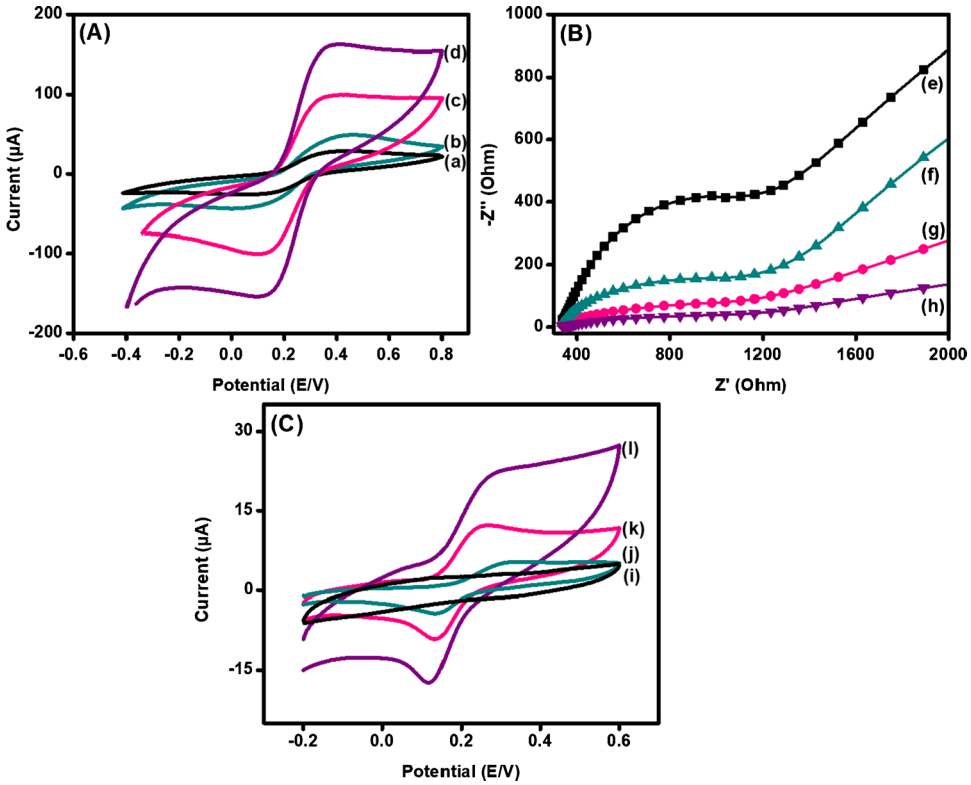


**Fig. 2** CV response (**A**) of a Bare GPE (a), IL/GPE (b), MXene/GPE (c), and IL-MXene/GPE (d); EIS (**B**) of the Bare GPE (e), IL/GPE (f), MXene/GPE (g), and IL-MXene/GPE (h) in 5 mM $(Fe(CN)6)^{4-/3-}$ (1:1). CV (**C**) of GPE modified with IL (i), Bare (j), MXene (k), and IL-MXene (l) in presence of 100 µM DA solution in the PBS ($pH = 7.4$). All the experiments were conducted at a scan rate of 100 $mVs^{-1}$

The electrochemical active surface areas of modified GPE electrodes were premeditated from the following Rendles-Sevick equation:

$$i_p = 2.69 \times 10^5 A n^{3/2} D_{red}{}^{1/2} C^* \nu^{1/2} \quad (1)$$

where, $I_p$, $A$, $n$, and $C$ correspond to anodic peak current, active surface area, electrons numbers involved in the oxidation of potassium ferro/ferri cyanide ($n = 1$), and the concentration of ferrocyanide ($5 \times 10^{-3}$ M), and $D_{red}$ and $v$ correspond to the diffusion coefficient of potassium ferrocyanide ($7.6 \times 10^{-6}$ cm$^2$ s$^{-1}$) and the scan rate ($100 \times 10^{-3}$ V), respectively. The electroactive surface area (EASA) was found to be 0.02, 0.04, 0.08, and 0.14 cm$^2$ for bare, IL, MXene, and IL-MXene, respectively. The larger active surface area of developed nano-adduct offered robust channeling of an electron across the interphase that eventually increased the electrocatalytic activity.

The electron transfer shuttling charge and surface resistance were further validated through EIS measurements. The resistance of bare GPE electrode ($R_{ct} = 547\ \Omega$) in Fig. 2B(e) decreased reasonably after deposition of IL ($R_{ct} = 339\ \Omega$), as shown in Fig. 2B(f). This fall in resistance was due to the electrical conductivity possessed by IL. However, the resistance of MXene-modified GPE ($R_{ct} = 188\ \Omega$) decreased further, as shown in Fig. 2B(g) which could be ascribed to the good electron transfer properties possessed by MXene due to exposed surface terminations. These findings are in good agreement with CV observations for electric responses of GPE, and GPE modified with IL, MXene, and IL-MXene.

Furthermore, the IL-MXene/GPE showed an explicit decrease in resistance ($R_{ct} = 144\ \Omega$), as revealed in Fig. 2B(h) owing to the combined properties of IL and MXene with higher electronic conductivity. Similarly, the imidazolium group also promoted electron transportation from the redox probe to the electrode surface.

We further explored the electrochemical proficiency of the developed interface towards 100 µM DA in PBS ($pH = 7.4$) in the potential bounds of (− 0.2 to 0.6 V), as seen from Fig. 2C. The reversible oxidation peak with minor variations was observed for all types of modified electrodes. The IL/GPE showed a low-peak current (5.1 µA) and a high-peak potential (0.3 V), as shown in Fig. 2C(i). However, the MXene/GPE exhibited a higher current (12.6 µA) with the lower peak potential (0.26 V), as shown in Fig. 2C(j). The increase in faradic current and decrease in peak potential were due to the surface-induced functional groups [50]. However, the IL-MXene/GPE depicted maximum faradic response (22.4 µA) at a lower potential (0.25 V), Fig. 2C(k). The improved response could be due to the ideal stability accomplished by conductive MXene stabilized with IL, incorporating a highly sensitive sensing interface.

Furthermore, CV was executed to examine the reaction kinetic process and surface activity at the integrated interface in presence of 80 µM DA at the scan rate in the range of 25 to 425 mVs$^{-1}$. The CV graphs exhibited a positive shift in potential with increasing scan rates as revealed in Fig. 3A. A linear relationship was attained for DA by plotting a graph between anodic current and scan rate, as shown in Fig. 3(B).

$$y = 0.11\nu\left(\frac{mV}{s}\right) + 2.67\left(R^2 = 0.995\right) \quad (2)$$

Besides, this a linear regression relation was developed by plotting a graph between the square root of scan rate and anodic peak current, as shown in Fig. S4A, proposing an adsorption-controlled process [51]. It could be ascribed to the fast kinetics of electrons and ions owing to the active surface area of IL supported conductive MXene interface.

$$I_P = 2.39\nu\left(\frac{mV}{s}\right) - 7.53(R^2 = 0.981) \quad (3)$$

Meanwhile, a linear plot was achieved between the natural log of scan rates vs. anodic peak currents, as shown in Fig. S4B.

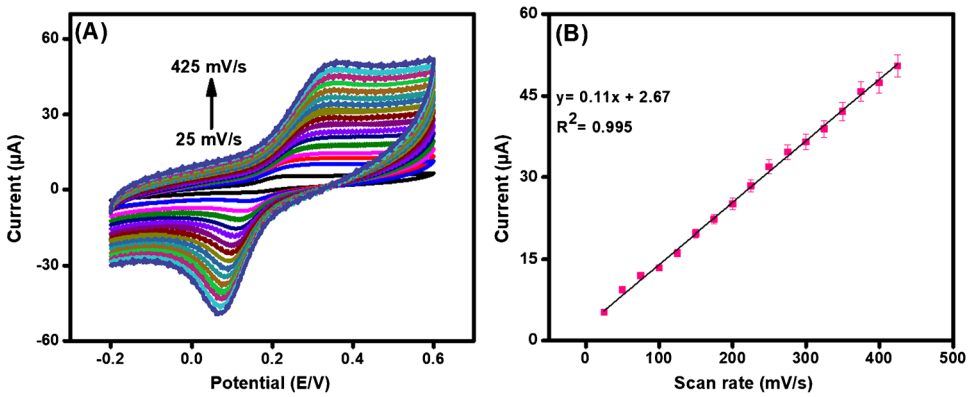


**Fig. 3** CV response (**A**) and its analogous linear graph (**B**) of IL-MXene/GPE in the presence of 80 µM DA in PBS (pH 7.4) at varying scan rates (25 to 425 mV/s)

$$lnI_P = 0.78\nu\left(\frac{mV}{s}\right) - 0.88(R^2 = 0.996) \quad (4)$$

Similarly, a graph has been drawn between the natural log of scan rate against peak potential ($E_p$) sourced a linear equation, as shown in Fig. S4C.

$$E_P = 0.03ln\nu + 0.11\left(R^2 = 0.955\right) \quad (5)$$

Based on these results, the standard rate constant for $K_s$ was calculated from the following Laviron's equation:

$$E_P = E_0 + 2.303\left(\frac{RT}{\alpha nF}\right)log\left(\frac{RTK_0}{\alpha nF}\right) + 2.303\left(\frac{RT}{\alpha nF}\right)log\nu \quad (6)$$

where, $E_p$ and $E_0$ are anodic and formal potentials of the integrated electrode system. $R$, $T$, $F$, $\alpha$, and $n$ correspond to the general gas constant, absolute temperature, Faraday constant, electron transfer coefficient, and number of electrons transferred, respectively. Meanwhile, the value of $\alpha n$ was premeditated from the slope of Fig. S4C. The values of $\alpha$ and number of electron transfer at the surface of IL-MXene/GPE were found to be 0.98 and 2.0, respectively, validating the two-electron/proton transferred steps based mechanism [52].

$$\log K_s = \alpha\log(1-\alpha) + (1-\alpha)log\alpha - \log\left(\frac{RT}{nF\nu}\right) - \alpha((1-\alpha)nF\Delta E_P/2.3RT \quad (8)$$

We employed DPV to examine the response of the developed IL-MXene/GPE-sensing interface against different concentrations of DA due to its magnified resolution, well-defined current response, and ability to decrease non-faradic response [56]. The DPV graphs, as shown in Fig. 4A and B, proposed the linear relationship between faradic current and increasing DA concentration [57]. Likewise, an increment in current along with a minor potential shift was also observed with increasing DA concentration, suggesting the improved surface coverage or adsorption of DA at the electrode interface [58, 59].

Additionally, we employed the current sensitive amperometry; a technique that is capable to achieve a lower detection limit with a reduced non-faradic response. The amperometric response of all modified electrodes (IL/GPE, MXene/GPE and IL-MXene/GPE) was investigated in the linear bounds of (100 µM–2 mM) DA concentrations in PBS at a working potential of 0.3 V, 0.26 V, and 0.25 V, respectively, as shown in Fig. 4C. Increasing concentration of analyte resulted in increased current response for all types of modified electrodes. However, the increment was phenomenal in the

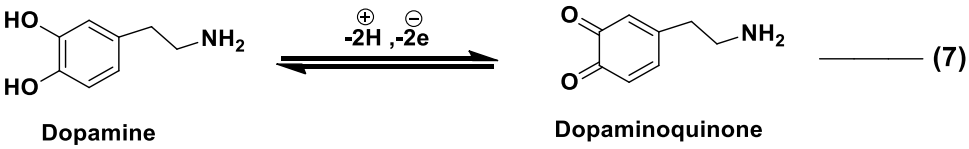


(7)

Additionally, the adsorption-controlled process at IL-MXene/GPE was due to the MXene loading on GPE to increase the active surface of the working electrode [53]. The multifunctional IL was loaded on the MXene interface via π-π interactions that not only enhanced ionic conductivity but also improved the biocompatibility for DA adsorption. The inherited negatively charged surface functional groups of MXene bound with the acidic methyl hydrogen of imidazole on IL [54]. Meanwhile, the imidazolium group of IL interacts with the DA. This infrastructure leads to a highly stable sensing surface that allowed the robust shuttling of electrons at the electrode–electrolyte interface. Consequently, the IL-MXene/GPE-oxidized DA to DA-*O*-quinone by the involvement of 2 electrons and protons (Eq. 7) leading to amplified faradic response with good sensitivity, as shown in Fig. 2C(l) and Scheme 1.

Besides, we have also calculated the electron transfer rate constant (ks) by employing Laviron's equation (Eq. 8) and the value for electron transfer rate constant for IL-MXene/GPE interface was found to be 0.74 $s^{-1}$: [55]

case of IL-MXene/GPE with a response time of 3 s, corroborating the high sensing capability of ionic liquid-stabilized MXene towards DA. Meanwhile, we obtained 2 linearities, as shown in linear graphs of DPV and amperometry. The lesser sensitivity at higher concentrations could be due to the ohmic drop and electrode fouling. With the increase in the concentration of DA, a greater number of oxidation products form and adsorb on the electrode surface which prevents diffusion and oxidation [60]. It can also be attributed to comparatively higher energy required for anodic stripping and ohmic drop at higher analyte concentrations as compared to the lower concentrations [61]. However, a good linear response was obtained compared with previously reported interfaces. The limit of detection (LOD) was calculated using Eq. S2 and found to be 702 nM ($S/N = 3$) for IL-MXene/GPE. Similarly, the sensitivity of the IL-MXene/GPE in DA was found to be 9.61 µA $\mu M^{-1}$ $cm^{-2}$. Interestingly, these results are in good competition with literature as presented in Table 1.

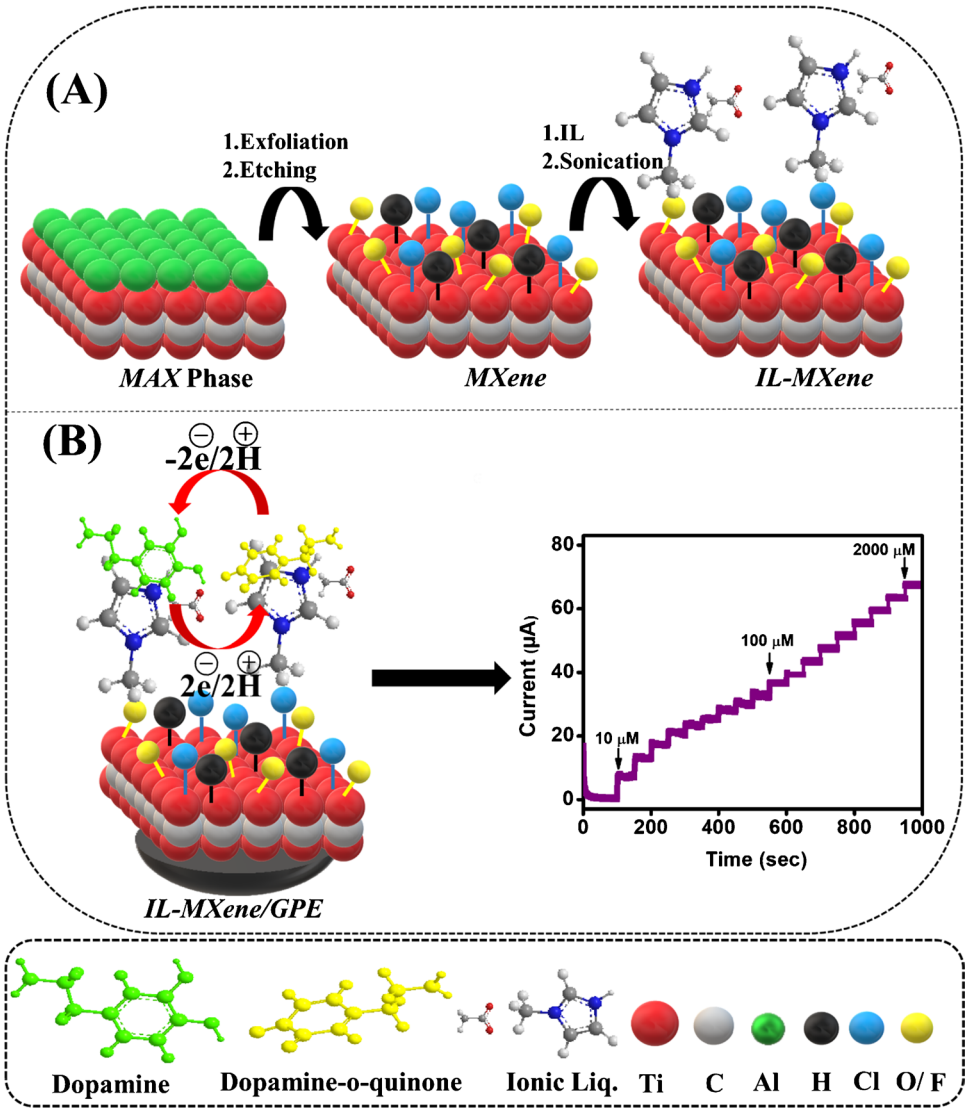


**Scheme 1** Schematic illustration of the IL-MXene/GPE fabrication and oxidative process towards non-enzymatic dopamine sensor

## Selectivity, repeatability, reproducibility, and stability of designed sensor

The prime challenge in sensor development is to selectively analyze the analyte of interest in the complex physiological medium containing coexisting interfering species. We selected a number of analytes as possible interfering species on the basis of their presence in biological systems and with respect to the similar electrochemical responses. We examined the selective efficiency of the integrated IL-MXene/GPE interface towards the electrochemical determination of DA on the same experimental protocol. The good amperometric current response of the transducing interface towards DA at working potential of 0.25 V was obtained, as shown in Fig. 5A. Interestingly, the insignificant current response was displayed after the addition of interfering species like glucose, cysteine, fructose, and urea even at much higher (500 μM) concentrations. Even, the negligible current response was shown in the case of uric acid and ascorbic acid which are electrochemically coherent species for DA. This noteworthy selective and specific response could be attributed to the good interactions between imidazolium nitrogen and DA [62].

The repeatability, reproducibility, and stability of the designed sensing interface were also examined and validated under the parallel conditions. The relative standard deviation was found to be 2.3% after recurrent utilization of the same electrode ($n = 10$), proposing the decent repeatability of the fabricated sensor, as exposed in Fig. 5B. This is due to the MXene interface that has the capability to show resistivity against the passivation and fouling of electrodes. The reproducibility of the integrated sensor was analyzed by comparing the response of 8 electrodes ($n = 3$) fabricated and analyzed in similar conditions, as revealed in Fig. 5C. The relative standard

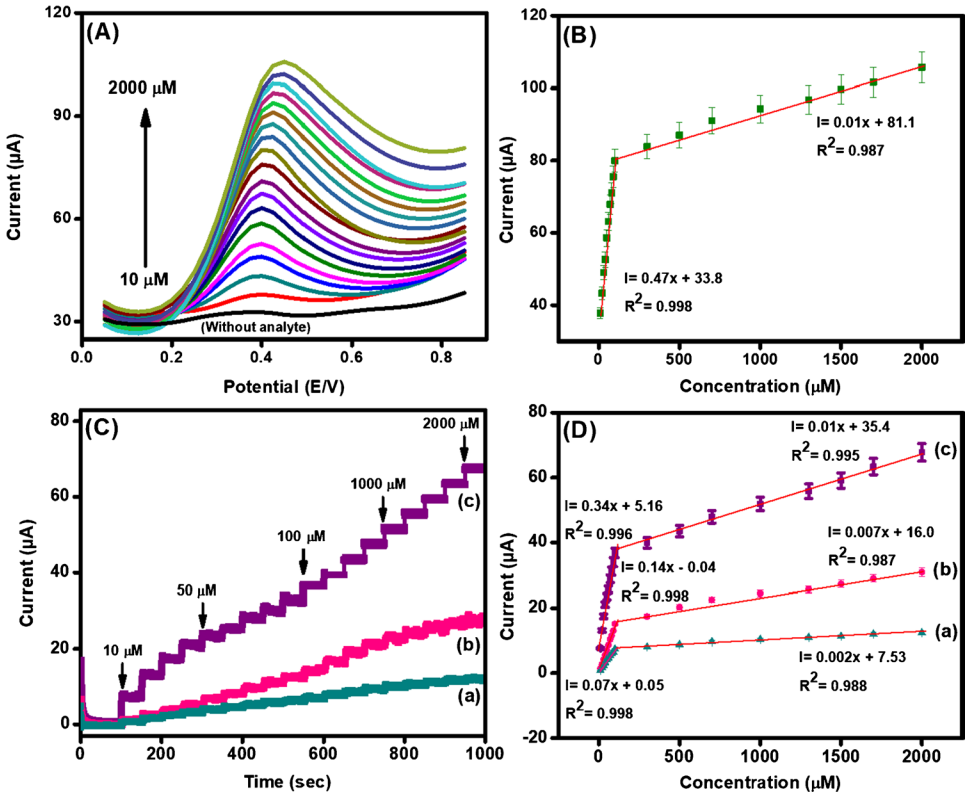


**Fig. 4** DPV response (**A**), analogous linear graph (**B**), amperometric response (**C**), and analogous linear graph (**D**) for IL-MXene/GPE in blank and at a concentration range from 10 to 2000 µM. All experiments were executed in PBS (pH 7.4) at a scan rate of 100 mV/s

**Table 1** Comparison of various sensors developed for DA detection with our designed IL-MXene/GPE

| Electrode material | Sensitivity (µA $\mu M^{-1}$ $cm^{-2}$) | LOD (nM) | Linear range (µM) | Reproducibility (RSD %) | Ref |
|---|---|---|---|---|---|
| GCE/N-rGO-180–8/NH3 | 1.82 | 410 | 0.5–150.0 | 6.22 | [65] |
| GNPs/MWCNTs | 2.06 | 70 | 0.4–5.7 | - | [66] |
| $RuS_2$/GCE | 1.80 | 73.8 | 10–80 | 6.40 | [67] |
| CdSe/CdS MSQDs | - | 96 | 0.5–15 | 7.20 | [68] |
| PEDOT-LSG | 0.22 | 330 | 1–150 | 2.70 | [69] |
| Ag@MoS2/GCE | - | 200 | 1–500 | - | [70] |
| $Ti_3C_2$/DNA/Pd/Pt@GCE | 1.05 | 30 | 0.2–1000 | - | [71] |
| SiTi/AuNP/CPE | 0.07 | 570 | 20–180 | 5.19 | [72] |
| pS-BIL MIP PeGE | - | 130 | 0.5–250 | - | [73] |
| H-ZIF/GCE | 0.32 | 12 | 0.25–590 | 5.50 | [74] |
| Cu/$Cu_xO$ | 0.51 | 1060 | 0.3–53 | - | [75] |
| carbon/ZnO-GCE | 0.57 | 106 | 0–300 | 3.99 | [60] |
| IL-MXene/GPE | 9.61 | 702 | 10–2000 | 1.90 | This work |

N-rGOs represented N-doped reduced graphene oxides; GNPs/MWCNTs represented gold nanoparticles immobilized on multi-walled carbon nanotubes; $RuS_2$ represented ruthenium(IV) disulfide; MSQD represented magic-sized quantum dots; PEDOT-LSG represented poly(3,4-ethylenedioxythiophene) immobilized laser scribed graphene; Ag@MoS2/GCE represented molybdenum disulfide nanosheet adorned with silver nanoparticles/glassy carbon electrode; *SiTi/AuNP*, silica-titania/gold nanoparticles; *pS-BIL NIP*, electrochemically formed thia-bilan molecularly imprinted polymer; *H-ZIF*, hollow zeolitic imidazolate

deviation was premeditated to be 1.9%. MXene's poor stability is the primary challenge for use of these efficient materials in practical applications as well as the fabrication of electrochemical sensors. Therefore, the storage stability of the developed sensing interface was also investigated, as shown in Fig. 5D. The fabricated sensor was stored at room temperature and was examined after every 2 days for 14 days. The relative standard

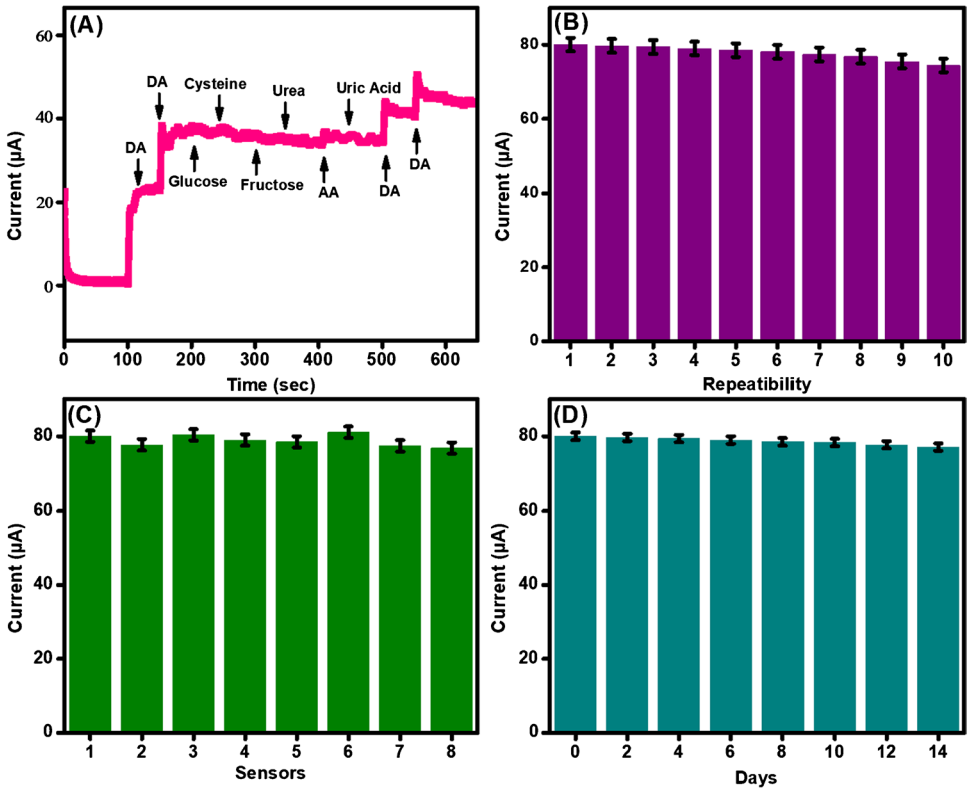


**Fig. 5** Amperometric response (**A**) of IL-MXene/GPE in the 40 μM DA (first 2 spikes), 20 μM DA (last 2 spikes) and 500 μM interfering molecules (glucose, cysteine, fructose, urea, ascorbic acid, and uric acid) in PBS (pH 7.4) at a scan rate of 100 mV/s. Repeatability (**B**) of IL-MXene decorated GPE for their response in DA for 10 times. Reproducibility (**C**) of 8 GPE fabricated electrodes with IL-MXene for their response in DA under analogous analytical parameters. Stability (**D**) of IL-MXene grafted GPE in DA for 14 days

deviation was revealed to be 1.3% verifying the long-term shelf life of the designed system.

### Real sample analysis on designed IL-MXene/GPE sensor

The practical development of electrochemical sensors is a great challenge, as the real sample possesses numerous biological interfering species along with DA. Hence, real sample analysis was performed on the as-developed sensing surface IL-MXene/GPE to explore the analytical performance practically, as shown in Fig. S5. Table S1 presents the recovery data of DA at four different spiked concentrations (10 μM, 50 μM, 80 μM, and 300 μM) in a phosphate buffer saline (pH 7.4). The assay has been described in the ESI file [63, 64]. Recoveries were calculated using Eq. S1 and found to be in the range of 98.3 to 100.0%. Moreover, to review the selectivity traits of the established electrochemical sensor, the standard addition method was employed to the serum samples and the regression equation was found to be $y\ (\mu A) = 0.07 \times (\mu M) + 0.05$. The good recoveries of the spiked DA serum samples corroborated the high accuracy of the designed sensor in the complex biological mediums.

## Conclusion

The study demonstrated the IL-MXene/GPE-based sensor for selective detection of DA. The developed strategy offers the development of an economically viable and highly stable MXene-based sensing interface. MXene can be uniformly deposited on GPE to enhance availability of active sites. Meanwhile, the multifunctional IL with biorecognition ability was used to engineer the MXene interface via electrostatic interactions. The developed platform exhibited good stability mitigating the stability issue of MXene-based sensors. The interface also improved the sensitivity and decreased detection limit of the system owing to conducting interfaces. The developed sensor also showed good reproducibility and practicability in human serum which would increase its potential for clinical applications.

**Supplementary Information** The online version contains supplementary material available at https://doi.org/10.1007/s00604-022-05162-3.

**Acknowledgements** UA acknowledges the financial support provided by HEC under the indigenous Ph.D. 5000 fellowship program (2PS5-179)/HEC/IS/2019) to pursue her Ph.D. at BZU Multan. MHN acknowledges the financial support provided by HEC (20-4993/R&D/HEC/14/614) and CUI (16-14/CRGP/CIIT/LHR/15/776).

## Declarations

**Conflict of interest** The authors have no relevant financial or non-financial interests to disclose.

## References


1. Sun F et al (2020) Next-generation GRAB sensors for monitoring dopaminergic activity in vivo. Nat Methods 17:1156–1166
2. Liu C, Goel P, Kaeser PS (2021) Spatial and temporal scales of dopamine transmission. Nat Rev Neurosci 22:345
3. Lu Z et al (2020) A dual-template imprinted polymer electrochemical sensor based on AuNPs and nitrogen-doped graphene oxide quantum dots coated on NiS2/biomass carbon for simultaneous determination of dopamine and chlorpromazine. Chem Eng J 389:124417
4. Shi Z et al (2021) Screen-printed analytical strip constructed with bacteria-templated porous N-doped carbon nanorods/Au nanoparticles for sensitive electrochemical detection of dopamine molecules. Biosens Bioelectron:113303
5. Bas SZ et al (2019) A novel electrochemical sensor based on metal ion infiltrated block copolymer thin films for sensitive and selective determination of dopamine. ACS Appl Nano Mater 2:7311–7318
6. Shu Y et al (2021) Isolated cobalt atoms on N-doped carbon as nanozymes for hydrogen peroxide and dopamine detection. ACS Appl Nano Mater 4:7954
7. Ma F et al (2020) Sonication-triggered rolling of Janus porous nanomembranes for electrochemical sensing of dopamine and ascorbic acid. ACS Appl Nano Mater 3:10032–10039
8. Gao F et al (2021) All-polymer free-standing electrodes for flexible electrochemical sensors. Sensors Actuators B Chem 334:129675
9. Kokulnathan T et al (2021) Rational confinement of yttrium vanadate within three-dimensional graphene aerogel: electrochemical analysis of monoamine neurotransmitter (dopamine). ACS Appl Mater Interfaces 13:10987–10995
10. Vázquez-Guardado A et al (2018) Enzyme-free plasmonic biosensor for direct detection of neurotransmitter dopamine from whole blood. Nano Lett 19:449–454
11. Huang C-W, Lu MS-C (2011) Electrochemical detection of the neurotransmitter dopamine by nanoimprinted interdigitated electrodes and a CMOS circuit with enhanced collection efficiency. IEEE Sens J 11:1826–1831
12. Wang P et al (2021) Scalable solution-processed fabrication approach for high-performance silver nanowire/MXene hybrid transparent conductive films. Nanomaterials 11:1360
13. Ma Y et al (2018) 3D synergistical MXene/reduced graphene oxide aerogel for a piezoresistive sensor. ACS Nano 12:3209–3216
14. Jiang Y et al (2018) Silver nanoparticles modified two-dimensional transition metal carbides as nanocarriers to fabricate acetycholinesterase-based electrochemical biosensor. Chem Eng J 339:547–556
15. Wu M et al (2021) Polylysine-modified MXene nanosheets with highly loaded glucose oxidase as cascade nanoreactor for glucose decomposition and electrochemical sensing. J Colloid Interface Sci 586:20–29
16 Wang Q et al (2020) Modified Ti3C2TX (MXene) nanosheet-catalyzed self-assembled, anti-aggregated, ultra-stretchable, conductive hydrogels for wearable bioelectronics. Chem Eng J 401:126129
17. Zheng Y et al (2021) Conductive MXene/cotton fabric based pressure sensor with both high sensitivity and wide sensing range for human motion detection and E-skin. Chem Eng J 420:127720
18. Tu X et al (2020) Mxene/carbon nanohorn/β-cyclodextrin-metal-organic frameworks as high-performance electrochemical sensing platform for sensitive detection of carbendazim pesticide. J Hazard Mater 396:122776
19. Zhong W et al (2021) MXene@ Ag-based ratiometric electrochemical sensing strategy for effective detection of carbendazim in vegetable samples. Food Chem 360:130006
20. Liu J et al (2019) MXene-Enabled electrochemical microfluidic biosensor: applications toward multicomponent continuous monitoring in whole blood. Adv Func Mater 29:1807326
21. Ma Y et al (2017) A highly flexible and sensitive piezoresistive sensor based on MXene with greatly changed interlayer distances. Nat Commun 8:1–8
22. Wang S et al (2021) Hierarchical design of waterproof, highly sensitive, and wearable sensing electronics based on MXene-reinforced durable cotton fabrics. Chem Eng J 408:127363
23. Kalambate PK, Sinha A, Li Y, Shen Y, Huang Y (2020) An electrochemical sensor for ifosfamide, acetaminophen, domperidone, and sumatriptan based on self-assembled MXene/MWCNT/chitosan nanocomposite thin film. Microchim Acta 187:1–12
24. Chen WY et al (2020) Surface functionalization of Ti3C2T x MXene with highly reliable superhydrophobic protection for volatile organic compounds sensing. ACS Nano 14:11490–11501
25. Luo J et al (2021) Superhydrophobic and breathable smart MXene-based textile for multifunctional wearable sensing electronics. Chem Eng J 406:126898
26. Xu Q et al (2021) Facile synthesis of hierarchical MXene/ZIF-67/CNTs composite for electrochemical sensing of luteolin. J Electroanal Chem 880:114765
27. Chen S et al (2021) Polydopamine bridged MXene and NH2-MWCNTs nanohybrid for high-performance electrochemical sensing of acetaminophen. Appl Surf Sci 570:151149
28. Nagles E, García-Beltrán O, Calderón JA (2017) Evaluation of the usefulness of a novel electrochemical sensor in detecting uric acid and dopamine in the presence of ascorbic acid using a screen-printed carbon electrode modified with single walled carbon nanotubes and ionic liquids. Electrochim Acta 258:512–523
29. Rauf S et al (2020) Ionic liquid coated zerovalent manganese nanoparticles with stabilized and enhanced peroxidase-like catalytic activity for colorimetric detection of hydrogen peroxide. Mater Res Express 7:035018
30. Li J et al (2017) A novel ionic liquid functionalized graphene oxide supported gold nanoparticle composite film for sensitive electrochemical detection of dopamine. RSC Adv 7:2315–2322
31. Kunpatee K, Traipop S, Chailapakul O, Chuanuwatanakul S (2020) Simultaneous determination of ascorbic acid, dopamine, and uric acid using graphene quantum dots/ionic liquid modified screen-printed carbon electrode. Sensors Actuators B Chem 314:128059
32. Pourtaheri E, Taher MA, Ali GA, Agarwal S, Gupta VK (2019) Electrochemical detection of gliclazide and glibenclamide on ZnIn2S4 nanoparticles-modified carbon ionic liquid electrode. J Mol Liq 289:111141
33. Boobphahom S, Ruecha N, Rodthongkum N, Chailapakul O, Remcho VT (2019) A copper oxide-ionic liquid/reduced graphene oxide composite sensor enabled by digital dispensing: non-enzymatic paper-based microfluidic determination of creatinine in human blood serum. Anal Chim Acta 1083:110–118
34. Yu L et al (2020) Ionic liquid combined with NiCo2O4/rGO enhances electrochemical oxygen sensing. Talanta 209:120515

35. Wang X et al (2014) Sensitive electrochemical detection of dopamine with a DNA/graphene bi-layer modified carbon ionic liquid electrode. Talanta 128:373–378
36. Sun W et al (2012) Poly (methylene blue) functionalized graphene modified carbon ionic liquid electrode for the electrochemical detection of dopamine. Anal Chim Acta 751:59–65
37. Chen S et al (2018) Polyoxometalate-coupled MXene nanohybrid via poly (ionic liquid) linkers and its electrode for enhanced supercapacitive performance. Nanoscale 10:20043–20052
38. Li M et al (2019) Element replacement approach by reaction with Lewis acidic molten salts to synthesize nanolaminated MAX phases and MXenes. J Am Chem Soc 141:4730–4737
39. Zarif F et al (2018) Ionic liquid coated iron nanoparticles are promising peroxidase mimics for optical determination of H 2 O 2. Microchim Acta 185:1–9
40. Amara U et al (2021) Self-assembled perylene-tetracarboxylic acid/multi-walled carbon nanotube adducts based modification of screen-printed interface for efficient enzyme immobilization towards glucose biosensing. Microchem J 165:106109
41. Riaz S, Feng W, Khan AF, Nawaz MH (2016) Sonication-induced self-assembly of polymeric porphyrin–fullerene: formation of nanorings. J Appl Polym Sci 133:43537
42. Alhabeb M et al (2017) Guidelines for synthesis and processing of two-dimensional titanium carbide (Ti3C2T x MXene). Chem Mater 29:7633–7644
43. Li Y et al (2020) A general Lewis acidic etching route for preparing MXenes with enhanced electrochemical performance in non-aqueous electrolyte. Nat Mater 19:894–899
44. Pu J-H et al (2020) A strain localization directed crack control strategy for designing MXene-based customizable sensitivity and sensing range strain sensors for full-range human motion monitoring. Nano Energy 74:104814
45. Han M et al (2016) Ti3C2 MXenes with modified surface for high-performance electromagnetic absorption and shielding in the X-band. ACS Appl Mater Interfaces 8:21011–21019
46. Ali A, Belaidi A, Ali S, Helal MI, Mahmoud KA (2016) Transparent and conductive Ti 3 C 2 T x (MXene) thin film fabrication by electrohydrodynamic atomization technique. J Mater Sci Mater Electron 27:5440–5445
47. Ling Z et al (2014) Flexible and conductive MXene films and nanocomposites with high capacitance. Proc Natl Acad Sci 111:16676–16681
48. Lu Z et al (2019) Ionic liquid/poly-l-cysteine composite deposited on flexible and hierarchical porous laser-engraved graphene electrode for high-performance electrochemical analysis of lead ion. Electrochim Acta 295:514–523
49. Varol TÖ et al (2019) Fabrication of graphene/azobenzene-perylene diimide derivative modified electrochemical sensors for the dopamine detection based on full factorial experimental design. Measurement 147:106867
50. Joshi S, Kamble VB, Kumar M, Umarji AM, Srivastava G (2016) Nickel substitution induced effects on gas sensing properties of cobalt ferrite nanoparticles. J Alloy Compd 654:460–466
51. Amara U et al (2021) Copper oxide integrated perylene diimide self-assembled graphitic pencil for robust non-enzymatic dopamine detection. RSC Adv 11:25084–25095
52. Kokulnathan T, Anthuvan AJ, Chen S-M, Chinnuswamy V, Kadirvelu K (2018) Trace level electrochemical determination of the neurotransmitter dopamine in biological samples based on iron oxide nanoparticle decorated graphene sheets. Inorg Chem Front 5:705–718
53. Amara U et al (2021) Perylene diimide/MXene-modified graphitic pencil electrode-based electrochemical sensor for dopamine detection. Microchim Acta 188:1–13
54. Sharifuzzaman M et al (2020) An electrodeposited MXene-Ti3C2Tx nanosheets functionalized by task-specific ionic liquid for simultaneous and multiplexed detection of bladder cancer biomarkers. Small 16:2002517
55. Zhou Y et al (2014) Selective determination of dopamine and uric acid using electrochemical sensor based on poly (alizarin yellow R) film-modified electrode. Anal Methods 6:3474–3481
56. Mercante LA et al (2015) Electrospun polyamide 6/poly (allylamine hydrochloride) nanofibers functionalized with carbon nanotubes for electrochemical detection of dopamine. ACS Appl Mater Interfaces 7:4784–4790
57. Ramachandran R, Leng X, Zhao C, Xu Z-X, Wang F (2020) 2D siloxene sheets: a novel electrochemical sensor for selective dopamine detection. Appl Mater Today 18:100477
58. Reddy S, Swamy BK, Jayadevappa H (2012) CuO nanoparticle sensor for the electrochemical determination of dopamine. Electrochim Acta 61:78–86
59. Hobbs CN, Johnson JA, Verber MD, Wightman RM (2017) An implantable multimodal sensor for oxygen, neurotransmitters, and electrophysiology during spreading depolarization in the deep brain. Analyst 142:2912–2920
60 Zhihua L et al (2021) Hypha-templated synthesis of carbon/ZnO microfiber for dopamine sensing in pork. Food Chem 335:127646
61. Prasad BB, Jauhari D, Tiwari MP (2013) A dual-template imprinted polymer-modified carbon ceramic electrode for ultra trace simultaneous analysis of ascorbic acid and dopamine. Biosens Bioelectron 50:19–27
62. Jiang L-C, Zhang W-D (2010) A highly sensitive nonenzymatic glucose sensor based on CuO nanoparticles-modified carbon nanotube electrode. Biosens Bioelectron 25:1402–1407
63. Yola ML (2021) Sensitive sandwich-type voltammetric immunosensor for breast cancer biomarker HER2 detection based on gold nanoparticles decorated Cu-MOF and Cu 2 ZnSnS 4 NPs/Pt/gC 3 N 4 composite. Microchim Acta 188:1–13
64. Karaman C, Karaman O, Atar N, Yola ML (2021) Electrochemical immunosensor development based on core-shell high-crystalline graphitic carbon nitride@ carbon dots and Cd 0.5 Zn 0.5 S/d-Ti 3 C 2 T x MXene composite for heart-type fatty acid–binding protein detection. Microchim Acta 188:1–15
65. Wiench P, González Z, Menéndez R, Grzyb B, Gryglewicz G (2018) Beneficial impact of oxygen on the electrochemical performance of dopamine sensors based on N-doped reduced graphene oxides. Sensors Actuators B Chem 257:143–153
66. Caetano FR, Felippe LB, Zarbin AJ, Bergamini MF, Marcolino-Junior LH (2017) Gold nanoparticles supported on multi-walled carbon nanotubes produced by biphasic modified method and dopamine sensing application. Sensors Actuators B Chem 243:43–50
67. Deepika J, Sha R, Badhulika S (2019) A ruthenium (IV) disulfide based non-enzymatic sensor for selective and sensitive amperometric determination of dopamine. Microchim Acta 186:480
68. de França CCL et al (2021) Development of novel paper-based electrochemical device modified with CdSe/CdS magic-sized quantum dots and application for the sensing of dopamine. Electrochim Acta 367:137486
69. Xu G, Jarjes ZA, Desprez V, Kilmartin PA, Travas-Sejdic J (2018) Sensitive, selective, disposable electrochemical dopamine sensor based on PEDOT-modified laser scribed graphene. Biosens Bioelectron 107:184–191
70. Sookhakian M, Basirun WJ, Goh BT, Woi PM, Alias Y (2019) Molybdenum disulfide nanosheet decorated with silver nanoparticles for selective detection of dopamine. Colloids Surf B Biointerfaces 176:80–86

71. Zheng J, Wang B, Ding A, Weng B, Chen J (2018) Synthesis of MXene/DNA/Pd/Pt nanocomposite for sensitive detection of dopamine. J Electroanal Chem 816:189–194
72. de Matos Morawski F et al (2021) A novel electrochemical platform based on mesoporous silica/titania and gold nanoparticles for simultaneous determination of norepinephrine and dopamine. Mater Sci Eng C 120:111646
73. Kaya HK et al (2021) A novel design thia-bilane structure-based molecular imprinted electrochemical sensor for sensitive and selective dopamine determination. Sensors Actuators B Chem 346:130425
74. Dong Y, Liu J, Zheng J (2021) A sensitive dopamine electrochemical sensor based on hollow zeolitic imidazolate framework. Colloids Surf A Physicochem Eng Asp 608:125617
75. Bahrami E, Amini R, Vardak S (2021) Electrochemical detection of dopamine via pencil graphite electrodes modified by Cu/CuxO nanoparticles. J Alloys Compd 855:157292